IGARSS 2025 - 2025 IEEE International Geoscience and Remote Sensing Symposium | 979-8-3315-0810-4/25/$31.00 ©2025 IEEE | DOI: 10.1109/IGARSS55030.2025.11244022

# DEEP LEARNING-BASED HIGH-RESOLUTION TIME-FREQUENCY DOMAIN RFI SUPPRESSION IN PASSIVE SYSTEMS

*A. M. Alam*[(1)], *M. Kurum*[(2)], *A. C. Gurbuz*[(1)]

[(1)] North Carolina State University, Raleigh, NC, USA
[(2)] University of Georgia, Athens, GA, USA

## ABSTRACT

This study presents a deep learning-based approach for detecting and mitigating radio frequency interference (RFI) at high-resolution time-frequency (TF) domain for microwave radiometry. The proposed work focuses on multi-signal scenarios, simulating diverse interference waveforms to reflect real-world conditions. High-resolution detection in the TF domain enables selective mitigation of only the RFI-affected portions of the spectrogram, preserving more non-RFI regions for accurate radiometric estimation. Residual noise power after RFI removal is analyzed to highlight the importance of RFI detection and mitigation within TF bins. To quantify the impact of mitigation, the resolution loss (RL) metric is utilized, assessing degradation in radiometric sensitivity. Additionally, Mean Absolute Percentage Error (MAPE) is calculated to evaluate discrepancies between actual and predicted noise power post-mitigation. A comparative analysis with the traditional spectral kurtosis method demonstrates that the proposed deep learning model achieves lower MAPE and RL across various power levels, preserving more uncontaminated TF bins, while ensuring robust RFI suppression. This study underscores the importance of balancing detection accuracy, noise preservation, and resolution sensitivity for effective RFI mitigation.

***Index Terms*—** Microwave Radiometry, Radio Frequency Interference, Deep Learning, Spectrum Coexistence, SMAP, Calibration. Time-Frequency Analysis

## 1. INTRODUCTION

Radio Frequency Interference (RFI) has emerged as a significant challenge for passive remote sensing systems [1]. Passive microwave radiometry, which relies on measuring natural thermal emissions, is particularly vulnerable to interference from anthropogenic sources such as wireless communication and radar systems [2]. These emissions are critical for applications like soil moisture estimation, freeze-thaw state detection, and other geophysical and atmospheric measurements [3]. Despite operating in protected spectral bands, radiometers often face interference from neighboring wireless systems or unknown sources.

Traditional RFI detection methods, such as kurtosis, pulse, and cross-frequency detection, rely on hand-engineered features and are designed to target specific types of interference [4, 5]. While these algorithms are effective in certain scenarios, their performance often degrades when faced with dynamically changing RFI characteristics like varying power levels, bandwidths, and duty cycles [6]. Additionally, traditional methods struggle to handle scenarios involving multiple overlapping signals within the same frequency band, where interference patterns become more complex and harder to distinguish. These methods typically lack robustness across different types of RFI and struggle to achieve high resolution in time-frequency (TF) domains. As a result, current solutions are inefficient, particularly for spectrum coexistence scenarios where preserving uncontaminated portions of the spectrum is critical. With future radiometers potentially coexisting in unprotected spectral bands, it becomes even more crucial to develop robust RFI detection and mitigation solutions that can adapt to diverse and evolving interference conditions.

In this study, we present a deep learning (DL)-based framework for RFI detection and mitigation, addressing some of the limitations of traditional methods. Unlike conventional approaches, the proposed method treats RFI detection as a high-resolution binary classification problem in the TF domain [7–12]. By leveraging synthetic datasets composed of diverse interference waveforms, the DL model is trained to accurately identify contaminated regions at the granularity of individual TF bins. The effectiveness of this approach is evaluated using metrics such as accuracy, precision, recall, Mean Absolute Percentage Error (MAPE) and Resolution Loss (RL), demonstrating superior performance compared to spectral kurtosis methods. This work underscores the potential of DL-based methods to preserve uncontaminated spectrum while providing robust interference suppression.

The remainder of the paper is organized as follows: data generation is detailed in Section 2, while the DL model RFI detection and mitigation is in Section 3. Results are provided in Section 4 and finally, a conclusion is drawn in Section 5.

This work was supported by National Science Foundation under Grant #2332661 and #2332662 titled " SWIFT-SAT: INtegrated Testbed Ensuring Resilient Active/Passive CoexisTence (INTERACT): End-to-End Learning-Based Interference Mitigation for Radiometers and NASA, Soil Moisture Active-Passive Mission Science Team, Grant #80NSSC25K7061."



Authorized licensed use limited to: University of Georgia. Downloaded on December 26,2025 at 14:35:11 UTC from IEEE Xplore. Restrictions apply.

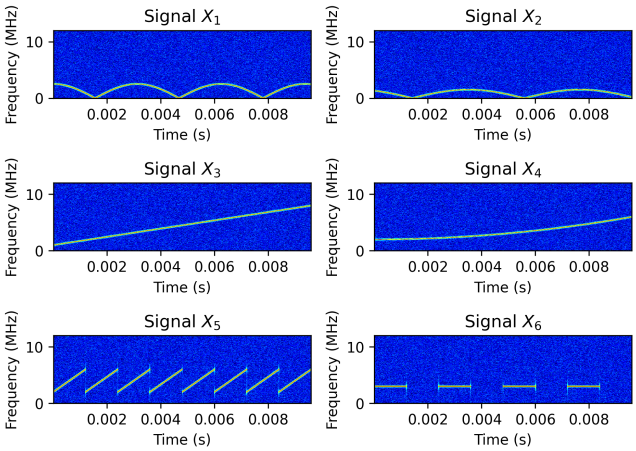


**Fig. 1**: High-resolution spectrogram examples from different RFI signal classes.

## 2. DATA GENERATION

### 2.1. Overview

The synthetic dataset incorporates six distinct waveform types, each representing typical forms of RFI encountered in microwave radiometry. These waveforms simulate signals generated by various stakeholders, such as communication systems, radar operations, and industrial equipment. Detailed descriptions of each waveform type and the potential sources are given that generate these RFI. The dataset used for training, validation, and testing consists of synthetic signals generated to simulate real-world scenarios. Each signal is represented as a spectrogram derived from the Short-Time Fourier Transform (STFT), with labels indicating RFI-contaminated portions in the frequency-time domain. Key parameters for data generation include a sampling rate of $f_s = 24\text{MHz}$, ensuring high temporal resolution, and a signal duration of $T = 9.6\text{ms}$ which is closely related to NASA's Soil Moisture Active Passive (SMAP) satellite specifications [13]. Each signal is transformed into the TF domain using a Short-Time Fourier Transform (STFT). A high-resolution TF is generated (i.e., 1024 frequency bins compared to 16 in SMAP), allowing RFI detections at higher resolutions.

### 2.2. Synthetic Signal Composition

Each signal consists of 2–6 randomly selected waveform types, generated using predefined mathematical formulations. Samples from six different waveform classes are illustrated in Fig. 1. The composite signal is expressed as:

$$x(t) = \sum_{i=1}^{N} x_i(t), \tag{1}$$

where $N$ is the number of waveforms, randomly chosen between 2 and 6, and $x_i(t)$ represents the $i$-th waveform contribution.

### 2.3. Waveform Definitions

Six types of waveforms are employed to create a diverse dataset of RFI signals. The signal formulations are as detailed next.

*2.3.1. Sinusoidal with Modulation (Waveform 1 and 2):*
These waveforms simulate narrowband interference commonly caused by communication systems like cellular networks or satellite communications. The sinusoidal modulation mimics periodic variations in transmitted power, characteristic of some broadcast systems.

$$x_1(t) = \sin\left(2\pi f \sin(320\pi t)\right), \tag{2}$$

$$x_2(t) = \sin\left(2\pi f \sin(240\pi t + 0.5)\right), \tag{3}$$

where $f$ is randomly selected from predefined frequency ranges.

*2.3.2. Quadratic and Cubic Chirp (Waveform 3 and 4):*
This waveform represents interference from radar systems operating with a quadratic frequency modulation for range detection.

$$x_3(t) = \sin\left(2\pi\left(f_0 t + \frac{f_1 - f_0}{2T} t^2\right)\right), \tag{4}$$

Cubic chirps model advanced radar or scientific instruments employing higher-order frequency modulations to enhance resolution or target discrimination.

$$x_4(t) = \sin\left(2\pi\left(f_0 t + \frac{f_1 - f_0}{3T^2} t^3\right)\right), \tag{5}$$

where $f_0$ and $f_1$ are the starting and ending frequencies, and $T$ is the signal duration.

*2.3.3. Linear Frequency Modulation (Waveform 5):*
A linear frequency-modulated signal, commonly referred to as a "chirp," is widely used in radar and sonar systems.

$$x_5(t) = \sin\left(2\pi\left(f_0 t + \frac{f_1 - f_0}{2T_{\text{PRI}}} t^2\right)\right), \tag{6}$$

where $T_{\text{PRI}}$ is the pulse repetition interval.

*2.3.4. Pulse Train (Waveform 6):*
Pulse train interference arises from periodic transmissions like those used in industrial machinery, telemetry, or pulsed radar systems. The alternation between active and silent intervals is typical of pulsed transmissions found in airspace surveillance radars and some industrial wireless applications.

$$x_6(t) = \begin{cases} \sin(2\pi f t), & t \in \text{active interval}, \\ 0, & t \in \text{silent interval}. \end{cases} \tag{7}$$

Figure 2 shows a spectrogram affected by RFI, with six distinct RFI sources overlapping within the same frequency band. These interference patterns, appearing as prominent features across both time and frequency, highlight the challenges involved in addressing RFI during signal processing.



Authorized licensed use limited to: University of Georgia. Downloaded on December 26,2025 at 14:35:11 UTC from IEEE Xplore. Restrictions apply.

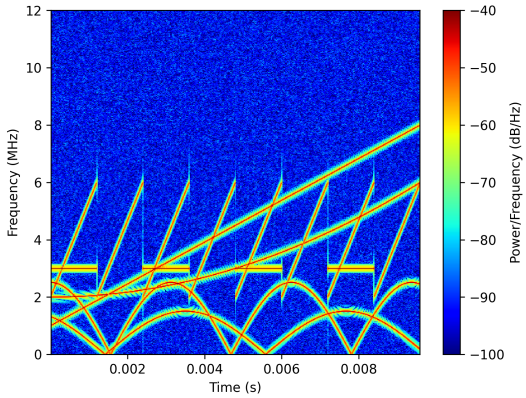


**Fig. 2**: Spectrogram showing RFI contamination with six distinct RFI sources overlapping within the same frequency band, highlighting their impact on the signal spectrum over time.

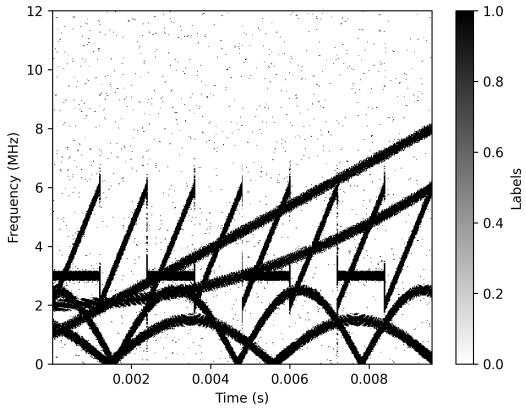


**Fig. 3**: Label map corresponding to the spectrogram, indicating the presence of six distinct RFI sources. The labels, displayed in grayscale, provide a binary representation (1 for RFI presence, 0 for absence) across time and frequency.

### 2.4. Noise Addition

Microwave radiometers are designed to measure natural thermal emissions from Earth's surface and atmosphere, which can be modeled as Gaussian noise under ideal, interference-free conditions. This natural noise forms the baseline for radiometric observations and is subsequently calibrated into brightness temperature and finally estimating geophysical parameters. To accurately simulate real-world conditions and facilitate RFI detection, Gaussian noise is added to the synthetic signals in the dataset. The noise power is calculated based on the interference-to-noise ratio ($\mathrm{INR_{dB}}$), ensuring that the noise levels reflect realistic conditions. The noise power is given by:

$$P_{\text{noise}} = \frac{P_{\text{signal}}}{10^{\mathrm{INR_{dB}}/10}}, \tag{8}$$

where $P_{\text{signal}}$ is the normalized signal power. For each sample in the dataset, $\mathrm{INR_{dB}}$ is arbitrarily selected from -10 dB, 0 dB, or 10 dB. The RFI-contaminated signal is expressed as:

$$x_{\text{rfi}}(t) = x(t) + x_n(t), \tag{9}$$

where $x_{rfi}(t)$ is the total radiometer received signal, $x(t)$ is the composite RFI signal, and $x_n(t) \sim \mathcal{N}(0, P_{\text{noise}})$ represents Gaussian noise with zero mean and variance equal to $P_{\text{noise}}$.

### 2.5. Spectrogram Calculation

The thermal noise signal is transformed into the frequency-time domain using the STFT. The spectrogram $S_x(f,t)$ is given by:

$$S_x(f,t) = \left| \sum_{n=0}^{N_{\text{FFT}}-1} x_{\text{n}}(n) w(n) e^{-j2\pi fn/N_{\text{FFT}}} \right|^2, \tag{10}$$

The analysis employs a Hann window function $w(n)$ with a size of 1024 FFT points and 50% overlap (512 points). The spectrogram is normalized within the sample to the range $[0, 1]$ for compatibility with the deep learning model:

### 2.6. Labeling

Binary labels are generated by thresholding the spectrogram using noise statistics. The threshold is defined as:

$$\text{Threshold}(f) = \mu(f) + 4\sigma(f), \tag{11}$$

where $\mu(f)$ and $\sigma(f)$ are the mean and standard deviation of the noise spectrogram. The binary mask is calculated as:

$$\text{Label}(f,t) = \begin{cases} 1 & \text{if } S_x(f,t) > \text{Threshold}(f), \\ 0 & \text{otherwise.} \end{cases} \tag{12}$$

Figure 3 shows the label map derived from the spectrogram, highlighting six distinct RFI sources. The grayscale values indicate RFI presence (1) or absence (0), effectively outlining interference patterns across time and frequency. This label map is considered the ground truth for DL model, while the spectrogram serves as the input.

## 3. DEEP LEARNING FRAMEWORK

The proposed method employs a convolutional neural network (CNN) architecture to detect RFI in microwave radiometers by processing spectrograms of radiometric data, where RFI-affected regions are labeled as 1 and uncontaminated areas as 0. The CNN comprises three main components: an encoder, a bottleneck, and a decoder. The encoder includes three convolutional layers with $3 \times 3$ kernels, ReLU activations, and progressively increasing filters (16, 32, 64) to capture hierarchical features. The bottleneck adds two $3 \times 3$ convolutional layers with 64 filters, allowing the model to learn complex interference patterns. The decoder restores spatial dimensions through three convolutional layers, reducing filters from 64 to 32, 16, and finally to 1. A sigmoid activation function produces a probability map indicating RFI contamination while preserving uncontaminated regions.



Authorized licensed use limited to: University of Georgia. Downloaded on December 26,2025 at 14:35:11 UTC from IEEE Xplore. Restrictions apply.

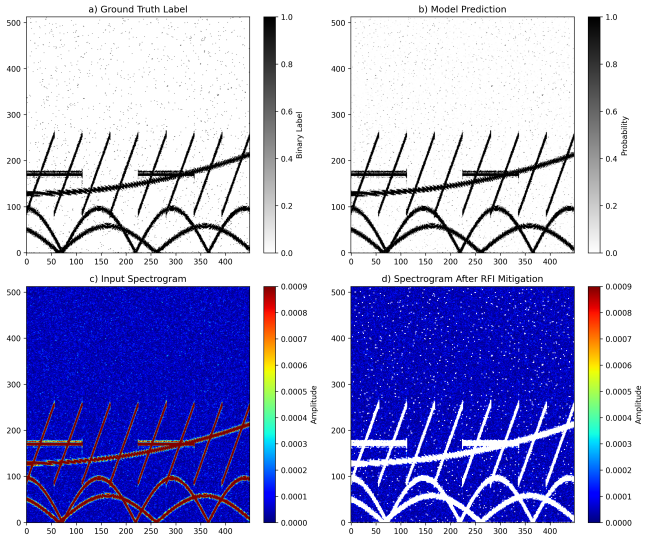


**Fig. 4**: DL performance analysis a) ground truth b) model prediction c) input spectrogram d) RFI removed spectrogram.

**Table 1**: RFI Detection Performance (%) Using DL

| INR | Accuracy | Precision | Recall | F1 Score |
|---|---|---|---|---|
| -10 | 92.13 | 90.47 | 91.08 | 90.77 |
| 0 | 95.24 | 91.64 | 91.58 | 91.60 |
| 10 | 96.37 | 93.89 | 92.70 | 93.29 |

## 4. RESULTS AND ANALYSIS

### 4.1. Evaluation Metrics

In this work, multiple performance metrics were employed to evaluate the effectiveness of RFI detection and mitigation. Accuracy, precision, and recall were used to measure the detection performance in identifying RFI-contaminated bins. Additionally, the mean absolute percentage error (MAPE) was calculated to quantify the error between the actual thermal noise power and the predicted noise power after RFI removal. Furthermore, the degradation of radiometric resolution, expressed as resolution loss (RL), was analyzed. RL quantifies the relative increase in radiometric resolution caused by the blanking process, which removes both RFI and a fraction of the thermal noise power. This process, while reducing the INR, leads to a loss of brightness temperature information, as the number of non-blanked bins ($M'$) is reduced compared to the total bins ($M$). RL is defined as RL $= \sqrt{M/M'} - 1$, where $M$ and $M'$ represent the total and non-blanked bins, respectively [4].

### 4.2. Performance Assessment

This section demonstrates the performance of DL-based models in detecting and mitigating RFI within spectrograms. Figure 4 illustrates the effectiveness of the DL model in identifying and suppressing RFI in the provided samples. By comparing Figures 4a and 4b, it is evident that the DL model accurately detects most of the RFI present in the spectrograms. Furthermore, by masking these contaminated regions, as shown in Figures 4c and 4d, the majority of the RFI is successfully removed, resulting in cleaner spectrograms.

**Table 2**: Comparison of DL and Spectral Kurtosis Algorithms for RFI Mitigation Across INR Levels

| Algorithms | INR | MAPE | RL |
|---|---|---|---|
| DL | -10 | 1.72 | 4.47 |
| | 0 | 1.88 | 4.68 |
| | 10 | 2.05 | 5.30 |
| Spectral Kurtosis | -10 | 9.34 | 7.86 |
| | 0 | 21.13 | 23.35 |
| | 10 | 25.47 | 30.35 |

With increasing INR levels, RFI becomes more prominent, making it easier for the model to detect and mitigate. This trend is reflected in Table 1, where higher INR levels correspond to improved precision, recall, and F1 scores. However, undetected RFI at higher INR levels poses a greater risk, as the residual interference left in the spectrogram can have a more significant impact on the final brightness temperature. Therefore, achieving high detection accuracy at elevated INR levels is critical for minimizing residual RFI and ensuring cleaner data quality. This highlights the importance of fine-tuning the model for scenarios with strong RFI signals.

The results in Table 2 illustrate that for the DL method, detection performance improves at higher INR levels, but the mitigation performance, as indicated by MAPE, decreases. Specifically, MAPE increases at higher INR levels. This can be attributed to the fact that missing RFI in high INR cases contributes more significantly to the estimated residual noise power after masking the contaminated regions. Similarly, RL is also higher at elevated INR levels for the same reason. Compared to the spectral kurtosis method, the DL approach demonstrates superior performance in both MAPE and RL across all INR levels. This suggests that the DL method is not only effective at preserving uncontaminated portions of the spectrum but also retains more TF bins compared to spectral kurtosis, making it a promising approach for potential spectrum coexistence solutions.

## 5. CONCLUSION

This study presents a DL-based framework for high-resolution RFI detection and mitigation in passive systems, demonstrating superior performance compared to traditional methods such as spectral kurtosis. By accurately identifying contaminated regions at the TF bin level, the proposed approach effectively preserves uncontaminated portions of the spectrum while minimizing resolution loss. The results underscore the potential of DL to address the challenges of RFI in multi-signal environments and support spectrum coexistence solutions. Future work will focus on evaluating the model with real-world radiometric data [14].



Authorized licensed use limited to: University of Georgia. Downloaded on December 26,2025 at 14:35:11 UTC from IEEE Xplore. Restrictions apply.

## 6. REFERENCES


[1] Sidharth Misra and Paolo de Matthaeis, "Passive remote sensing and radio frequency interference (rfi): An overview of spectrum allocations and rfi management algorithms [technical committees]," *IEEE Geoscience and Remote Sensing Magazine*, vol. 2, no. 2, pp. 68–73, 2014.

[2] Sidharth Misra, Priscilla N Mohammed, Baris Guner, Christopher S Ruf, Jeffrey R Piepmeier, and Joel T Johnson, "Microwave radiometer radio-frequency interference detection algorithms: A comparative study," *IEEE Transactions on Geoscience and Remote Sensing*, vol. 47, no. 11, pp. 3742–3754, 2009.

[3] F. T. Ulaby, R. K. Moore, and A. K. Fung, *Microwave Remote Sensing: Active and Passive. Volume 1 - Microwave Remote Sensing Fundamentals and Radiometry*, vol. 1, Artech House, Norwood, MA, 1981.

[4] Jorge Querol, Raul Onrubia, Alberto Alonso-Arroyo, Daniel Pascual, Hyuk Park, and Adriano Camps, "Performance assessment of time–frequency rfi mitigation techniques in microwave radiometry," *IEEE Journal of Selected Topics in Applied Earth Observations and Remote Sensing*, vol. 10, no. 7, pp. 3096–3106, 2017.

[5] Baris Guner, Joel T Johnson, and Noppasin Niamsuwan, "Time and frequency blanking for radio-frequency interference mitigation in microwave radiometry," *IEEE Transactions on Geoscience and Remote Sensing*, vol. 45, no. 11, pp. 3672–3679, 2007.

[6] Jeffrey R Piepmeier, Joel T Johnson, Priscilla N Mohammed, Damon Bradley, Christopher Ruf, Mustafa Aksoy, Rafael Garcia, Derek Hudson, Lynn Miles, and Mark Wong, "Radio-frequency interference mitigation for the soil moisture active passive microwave radiometer," *IEEE Transactions on Geoscience and Remote Sensing*, vol. 52, no. 1, pp. 761–775, 2013.

[7] Priscilla N Mohammed and Jeffrey R Piepmeier, "Microwave radiometer rfi detection using deep learning," *IEEE Journal of Selected Topics in Applied Earth Observations and Remote Sensing*, vol. 14, pp. 6398–6405, 2021.

[8] A. M. Alam, A. C. Gurbuz, and M. Kurum, "Smap radiometer rfi prediction with deep learning using antenna counts," in *IGARSS 2022 - 2022 IEEE International Geoscience and Remote Sensing Symposium*, 2022, pp. 8016–8019.

[9] Imara Mohamed Nazar and Mustafa Aksoy, "Radio frequency interference detection in passive microwave remote sensing using one-class support vector machines," *IEEE Journal of Selected Topics in Applied Earth Observations and Remote Sensing*, 2023.

[10] Ahmed Manavi Alam, Mehmet Kurum, and Ali C Gurbuz, "Radio frequency interference detection for smap radiometer using convolutional neural networks," *IEEE Journal of Selected Topics in Applied Earth Observations and Remote Sensing*, vol. 15, pp. 10099–10112, 2022.

[11] Raúl Díez-García, Adriano Camps, and Hyuk Park, "Rfi mitigation in microwave radiometry using the karhunen–loève transform," *IEEE Transactions on Geoscience and Remote Sensing*, vol. 61, pp. 1–13, 2023.

[12] A. M. Alam, M. Kurum, and A. C. Gurbuz, "High-resolution radio frequency interference detection in microwave radiometry using deep learning," in *IGARSS 2023 - 2023 IEEE International Geoscience and Remote Sensing Symposium*, 2023, pp. 6779–6782.

[13] Jeffrey Piepmeier, Priscilla Mohammed, Giovanni De, Amici Ed Kim, Jinzheng Peng, and Chris Ruf, "Soil Moisture Active Passive (SMAP) Algorithm Theoretical Basis Document (ATBD) SMAP Calibrated, Time-Ordered Brightness Temperatures L1B TB Data Product," 2014.

[14] Ahmed Manavi Alam, Md Mehedi Farhad, Walaa Al-Qwider, Ali Owfi, Mohammad Koosha, Nicholas Mastronarde, Fatemeh Afghah, Vuk Marojevic, Mehmet Kurum, and Ali C Gurbuz, "A physical testbed and open dataset for passive sensing and wireless communication spectrum coexistence," *IEEE Access*, 2024.




Authorized licensed use limited to: University of Georgia. Downloaded on December 26,2025 at 14:35:11 UTC from IEEE Xplore. Restrictions apply.